

Orientation and microstructure in sheared Brownian suspensions of anisotropic dicolloidal particles

Amit Kumar[†] and Jonathan J. L. Higdon^{*}

Department of Chemical and Biomolecular Engineering
University of Illinois at Urbana-Champaign, Urbana, IL 61801, USA

July 24, 2012

Abstract

Orientation and microstructure are investigated in sheared Brownian suspensions of hard dicolloidal particles, with the dicolloids modeled as two fused spheres of varying radii and center to center separations. Two different particle shapes named homonuclear (aspect ratio 1.1) and fused-dumbbells (aspect ratio 1.5) were considered. Hydrodynamic interactions between the particles were computed with a modified lubrication model called Fast Lubrication Dynamics. Studies were conducted for a wide range of volume fractions between $0.3 \leq \phi \leq 0.5$ and Péclet numbers between $0 \leq Pe \leq 1000$. The microstructure was found to be disordered at all volume fractions, though signatures of weak string like ordering were evident particularly in $\phi = 0.5$ homonuclear suspensions at intermediate to high shear rates (Pe in the range $10 - 100$). Complex orientation behavior was observed as a function of shape, shear rates, and volume fractions. At very low shear rates, random orientation distribution was observed in all cases. At the highest shear rates, orientation distribution in suspensions of homonuclear particles exhibited a shift towards an alignment with the vorticity axis at all volume fractions, while in suspensions of fused-dumbbells it exhibited a shift away from the vorticity axis at low volume fractions and a negligible shift at higher volume fractions. The orientation behavior is further characterized by examining the orientation distribution in the velocity–gradient plane – in this case an increased particle alignment with the velocity axis is generally observed with increasing volume fractions, but not universally with increasing shear rates. Mechanistic origins for the complex orientation behavior as a function of shear rate, volume fraction, and particle shape is described.

1 Introduction

In recent times anisotropic particles have attracted considerable interest in a wide range of fields. This surge in interest is arguably fueled by the recent synthesis of a variety of novel

[†] Present address: Department of Chemical and Biological Engineering, University of Wisconsin-Madison

^{*}Corresponding author. Email: jhigdon@illinois.edu



Figure 1: Examples of dicolloidal particles investigated in the current work. The two particle shapes are named homonuclear and fused-dumbbell particles as noted in the figure.

particle shapes^{1,2}, which themselves are enabled by the recent advances in particle synthesis techniques. Sizes of these particles are usually in the nanometer range with $O(100)$ nm being a typical size. Many applications have been proposed for these anisotropic particles; some prominent examples include their assembly into advanced nanostructured materials³ and for drug delivery^{4,5} among others. An interesting class of recently synthesized anisotropic particles are the dicolloidal particles^{6,7,8}, whose geometry is closely approximated by the union of two intersecting spheres of varying radii and center to center separations. Figure (1) illustrates several dicolloidal particle shapes examined in the present effort. A significant feature of dicolloidal particles is its low aspect ratio (AR) with an upper bound of 2.0. Owing to this low aspect ratio, mildly aspherical dicolloids often exhibit microstructural and rheological behavior similar to that in suspensions of spheres. However, in addition to the positional microstructure, suspensions of dicolloids possess distinct orientational microstructure. The goals of present work are to characterize both the orientational and the positional microstructure in sheared suspensions of *Brownian* dicolloidal particles. This continues our previous work on dicolloidal particles where we investigated the orientational and positional microstructure in sheared *non-Brownian* suspensions⁹. We review some of the important observations in this study below. In addition, we review below other pertinent literature on the orientation behavior in sheared suspensions of anisotropic particles.

In the absence of non-hydrodynamic effects (such as Brownian motion or electrostatic forces), Jeffery¹⁰ showed that a single spheroid (or more generally an ellipsoid) in a linear shear flow would rotate indefinitely in a single parameter family of closed orbits, commonly known as the Jeffery orbits. The parameter characterizing an orbit is called the orbit constant C whose value varies from $C = 0$ for particle director aligned with the vorticity axis to $C = \infty$ for particle alignment in the velocity-gradient plane. For an axisymmetric body, such as a spheroid or a dicolloid, its orientation may be specified by spherical coordinates (φ, θ) where θ measures the angle between the particle director and z axis, while φ is angle between the director and the y axis measured clockwise in the $x - y$ plane (see Fig. 2). The evolution of the orientational angles (φ, θ) with time t is given in terms of the orbit constant C by

$$\tan \varphi = r_s \tan \left(\frac{\dot{\gamma} t}{r_s + 1/r_s} + \kappa \right), \quad (1a)$$

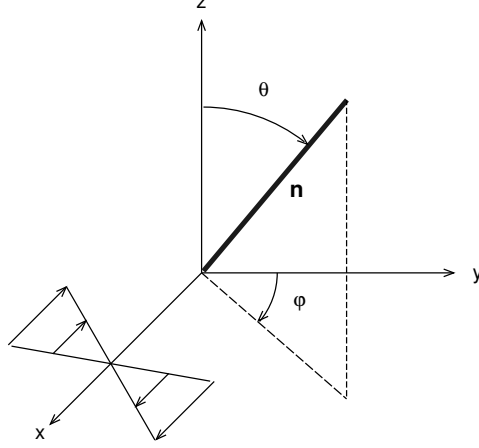


Figure 2: Definition of the spherical polar coordinate θ and the azimuthal angle φ .

$$\tan \theta = \frac{Cr_s}{\sqrt{r_s^2 \cos^2 \varphi + \sin^2 \varphi}}, \quad (1b)$$

where $\dot{\gamma}$ is the shear rate, r_s is the aspect ratio of the spheroid, while κ denotes the initial phase in the orbit. A particularly simple limit is that of a spherical particle ($r_s = 1$), in which case Jeffery's orbits corresponds to lines of constant θ (more specifically, $\theta = \tan^{-1} C$). Later, Bretherton¹¹ showed that in a linear shear flow most axisymmetric bodies, which includes dicolloids, will also rotate in Jeffery orbits with r_s in the equations above replaced by an effective aspect ratio r_e of the particle. It can be shown that the rate of rotation of a particle in any given orbit is non-uniform, such that its director spends a greater fraction of the time aligned in the velocity–vorticity plane in comparison to the gradient–vorticity plane. As such, under shear, a single non-Brownian anisotropic particle by itself will exhibit an enhanced time-averaged flow alignment (parallel to the velocity axis) in conjunction with a reduced gradient alignment (henceforth, by particle alignment we imply particle director alignment). On the other hand, the time-averaged vorticity alignment is mostly determined by the initial orientation of the particle; the initial orientation sets the orbit constant C , and the vorticity alignment does not change appreciably with time in any given orbit for particles with small degree of anisotropy.

The effect of Brownian motion on the orientation behavior of axisymmetric particles have been characterized in several theoretical studies in the limit of infinite dilution, i.e., non-interacting particle suspensions. Leal and Hinch¹² investigated the orientation distribution in suspensions of spheroids in the limit of very weak Brownian motion. The key argument in this study was that the rotation of a particle in any given Jeffery's orbit is unaltered when the Brownian motion is very weak. However, after sufficiently long times, the first effect of the weak Brownian motion will be to yield steady state distributions across orbits independent of the initial state of the suspension. Since the rate of rotation of a particle in any given orbit is unchanged, this result implies an enhanced particle alignment with the

velocity axis and a reduced particle alignment with the gradient axis, say, in comparison to an isotropic distribution. In an earlier study⁹, we showed that in the limit of weak Brownian motion, the particle alignment with the vorticity axis remains approximately isotropic for dicolloids. Hinch and Leal¹³ later extended their previous analysis to include higher order approximations, though still in the weak Brownian limit. This study, in comparison to Jeffery's solution, showed an enhanced probability at orientations just prior to complete flow alignment, in conjunction with a reduced probability at orientations just after complete flow alignment. This behavior results from the fact that the Brownian motion causes diffusion away from the highly populated flow aligned states, which, to first approximation, occurs with equal probability towards the pre flow aligned state and post flow aligned state. The advection, on the other hand, causes particle motion in a single direction of the undisturbed Jeffery's orbit. The balance between these two effects leads to the aforementioned probability distribution.

In the limit of strong Brownian motion, the orientation distribution in non-interacting suspensions of axisymmetric particles is provided by, e.g., Brenner¹⁴. At equilibrium, as could be expected, the orientation distribution was found to be isotropic. The first effect of the weak flow is to enhance the orientation probability around the extensional axis of the shear flow and a reduced probability along its compressional axis. The effect of shear flow is understood by noting that the overall flow in this case can be expressed as a sum of an extensional component and a rotational component. The rotational component has no effect at the leading order as the rate of rotation of the particle due to this component is uniform and the initial distribution, i.e., at equilibrium, isotropic. The effect of the extensional component of the flow is to rotate the particle away from the compressional axis towards alignment with the extensional axis, which explains the above observation. At higher order approximations, both the extensional as well as the rotational component of the flow will contribute. The effect of the rotational component of the flow will be to rotate the orientation distribution clockwise, thereby bringing the probability maxima closer to the velocity axis and the probability minima closer to the gradient axis. At very high shear rates, it can be expected that the weak Brownian limit discussed above will be reached, i.e., the region of maximum orientation probability will coincide with the velocity axis, while the region of minimum orientation probability will coincide with the gradient axis.

There have been relatively few studies on the orientation behavior in Brownian suspensions of anisotropic particles at finite concentrations. Some are discussed next. Meng and Higdon¹⁵ investigated the orientation behavior in concentrated Brownian suspensions of plate-like particles (AR between 3 and 7) via an extension of the Stokesian Dynamics technique. Their studies indicate an increasing particle alignment in the velocity-vorticity plane with increasing shear rates, volume fractions and aspect ratios. Egres et al.¹⁶ experimentally measured flow alignment in suspensions of ellipsoids of comparatively lower aspect ratios (AR between 2 and 7). This study showed that the flow alignment (parallel to velocity axis) was preferred at all shear rates with the maximum in flow alignment coinciding with the onset of shear thickening.

At even higher shear rates, a decrease in flow alignment was observed. This study also indicated an increased flow alignment with higher particle loadings as well as aspect ratios. The authors attributed the decrease in flow alignment at high shear rates to the formation of hydro-clusters, which will have a smaller degree of anisotropy than the constituent particle itself; this reduction in the effective anisotropy explains the decrease in particle flow alignment. Besides the studies noted above, there have also been many other studies on the orientation behavior in suspensions of high aspect ratio non-Brownian fibers, which is of limited interest here. For a detailed survey of such suspensions the reader is referred to our earlier publication⁹.

We recently investigated the orientation behavior in sheared non-Brownian suspensions of dicolloidal particles using the Stokesian dynamics technique⁹. This study explored the effect of particle shape as well as volume fraction. Two of the particle shapes investigated in this study are shown in Fig. (1). As noted in the figure, the two particles shapes, both of which are symmetric dicolloids, are named homonuclear and fused-dumbbell particles. The geometric aspect ratio of these two particles are $AR = 1.1$ and $AR = 1.5$, respectively. In this study it was shown that, at low volume fractions, both the particle shapes exhibited an orientation drift away from the vorticity axis towards the velocity-gradient plane. This drift was considerably higher for the fused-dumbbell particle than the homonuclear particle. The origin of this behavior was attributed to non-uniform fluctuations in the orientation space – particles aligned with the vorticity axis were found to undergo stronger fluctuations in its orientation as it underwent collisions with other particles. As discussed in Shaqfeh and Koch¹⁷, non-uniform fluctuations in the orientation space will result in a drift away from orientations with stronger fluctuations in agreement with the observations. At higher volume fractions, an orientation drift towards the vorticity axis away from the velocity-gradient plane was observed. The drift towards the vorticity axis was higher for the homonuclear particles than for the fused-dumbbell particles. In suspensions of force free and torque free particles, as is approximately the case in non-Brownian suspensions with a very short range repulsive force, the particle angular velocity can be directly related to the hydrodynamic stresslets, which refers to the symmetric part of the first moment of the fluid force on the particle. Indeed, it was shown that the particle drift towards the vorticity axis was correlated with the hydrodynamic stresslet, in particular with the second normal difference component of the stresslet⁹. In non-Brownian suspensions, the second normal stress differences are negative^{9,18}, which was shown to drive the orientation distribution towards an enhanced vorticity alignment. It is interesting to note that, in a non-Newtonian second order fluid, Leal¹⁹ showed that a high aspect ratio fiber subjected to shear will also drift towards vorticity alignment if second normal stress coefficient of the fluid is negative.

In the present effort, we will conduct numerical simulations for the dynamics of sheared suspensions of Brownian dicolloids. The hydrodynamic interactions as well as the Brownian motion of the particle are computed using the Fast Lubrication Dynamics (FLD) algorithm^{20,21}. The FLD algorithm is an approximation of the well known Stokesian Dynamics

technique^{22,23}. In the FLD algorithm, the overall resistance tensor is expressed as the sum of a pairwise lubrication term and a novel isotropic resistance term chosen so as to match the mean particle mobility from the more detailed Stokesian Dynamics. Using this algorithm we investigate the orientation and microstructure in Brownian hard dicolloidal particle suspensions as a function of shear rate and volume fraction. Two different particle shapes are considered here: the homonuclear and the fused-dumbbell particle. The microstructure is found to lack any long range order in the range of volume fraction investigated ($0.3 \leq \phi \leq 0.5$), though hints of weak string like ordering becomes evident at the highest volume fraction over a range of shear rates, especially in suspensions of homonuclear particles. The particle orientation is found to be random at low shear rates in all cases. At the highest shear rates, orientation distribution in suspensions of homonuclear particles exhibits a shift towards an alignment with the vorticity axis at all volume fractions, while in suspensions of fused-dumbbells it exhibits a shift away from the vorticity axis at low volume. The orientation distribution in the velocity–gradient plane shows an increased flow alignment with increasing volume fractions for both the particle shapes. The flow alignment is also found to increase with increasing shear rates at lower volume fractions, though, at higher volume fractions, this is not necessarily the case. The mechanism responsible for these orientation distributions with shear rate, volume fraction, and particle shape is described in light of previous studies on non-Brownian and strongly Brownian suspensions.

The organization of this article is as follows. In Sec. (2) we present the Fast Lubrication Dynamics technique for computing the hydrodynamic and Brownian forces on the particles. The solution procedure for computing the unknown velocities and angular velocities of the particles is also discussed here. Next, in Sec. (3.1), the results for the microstructure as a function of volume fraction, shear rate and particle shape is presented. Following this, the orientation behavior is characterized in Sec. (3.2). Concluding remarks are lastly presented in Sec. (4).

2 Formulation

The motion of Brownian particles in a viscous fluid can be described by Newton’s second law written as

$$\mathbf{m} \cdot \frac{d\mathbf{U}}{dt} = \mathbf{F}^H + \mathbf{F}^B + \mathbf{F}^P, \quad (2)$$

where \mathbf{m} is the mass/moment of inertia tensor of the particles, \mathbf{U} is the generalized velocity/angular velocity vector, while \mathbf{F}^H , \mathbf{F}^B , and \mathbf{F}^P are the generalized force/torque vectors arising respectively from the hydrodynamic stress in the fluid, stochastic Brownian motion, and interparticle interactions. Here the vectors \mathbf{U} , \mathbf{F}^H , \mathbf{F}^B and \mathbf{F}^P are $6N_p$ vectors where N_p is the number of particles in the system; the mass/moment of inertia \mathbf{m} is a $6N_p$ square block diagonal matrix where each 6×6 block consists of the mass and moment of inertia tensor of each individual particle. We assume that the particle size is small, and the inertial effects are

negligible. With this assumption, the left hand side of (2) is zero, and the sum of the forces and torques on each individual particle must be zero at every instant of time:

$$\mathbf{F}^H + \mathbf{F}^B + \mathbf{F}^P = 0. \quad (3)$$

We discuss next the numerical calculation of the above three type of forces, i.e., \mathbf{F}^H , \mathbf{F}^B , and \mathbf{F}^P .

2.1 Hydrodynamic force (\mathbf{F}^H)

Owing to its small size, the fluid motion around the particles is governed by the Stokes equations. In these low Reynolds number flows, the hydrodynamic force on each particle is a linear function of the fluid velocity and may be determined from the solution of the governing equations for a specified set of particle configurations, particle velocities and of a prescribed undisturbed flow field. The linear relationship may be expressed in terms of a configuration dependent N_p body resistance tensor \mathbf{R} as follows:

$$\begin{pmatrix} \mathbf{F}^H \\ \mathbf{S}^H \end{pmatrix} = \mathbf{R} \cdot \begin{pmatrix} \mathbf{U}^\infty - \mathbf{U} \\ \mathbf{E}^\infty \end{pmatrix}. \quad (4)$$

In the above equation, a homogeneous undisturbed linear shear flow is assumed which determines the generalized velocity/angular velocity \mathbf{U}^∞ evaluated at the center of each particle and the uniform rate of strain tensor denoted by \mathbf{E}^∞ . \mathbf{F}^H is the usual force/torque $6N_p$ vector and \mathbf{S}^H denotes the stresslets on the particle, the symmetric part of the first moment of the force on each particle, and can be expressed by a $5N_p$ vector.

In a previous effort²³, we developed a Stokesian dynamics technique to approximate the resistance tensor \mathbf{R} in suspensions of non-spherical particles including dicolloids. In the Stokesian Dynamics approach, the total resistance tensor \mathbf{R} in Eq. (4) is expressed by the following approximation:

$$\mathbf{R} = \mathbf{R}^{MB} + \mathbf{R}^{LB}, \quad (5)$$

where \mathbf{R}^{MB} is a many-body resistance tensor accurate for widely separated particles. When particles come near contact however, the small particle gaps lead to strong interactions with \mathbf{R} diverging at contact. The many body resistance tensor cannot capture this singular behavior due to the truncated multipole expansion employed in its calculation, hence, a correction term is added to account for the missing terms. This correction tensor denoted by \mathbf{R}^{LB} is based on asymptotic lubrication theory for nearly touching particles. Unlike \mathbf{R}^{MB} , \mathbf{R}^{LB} is a sparse matrix as the lubrication interactions affect only near neighbors, and most importantly, the asymptotic lubrication contributions are pairwise additive as the interaction is highly localized around the point of contact. In the Stokesian Dynamics technique the bulk of the computational cost is associated with the calculation of the far-field many-body interactions. However,

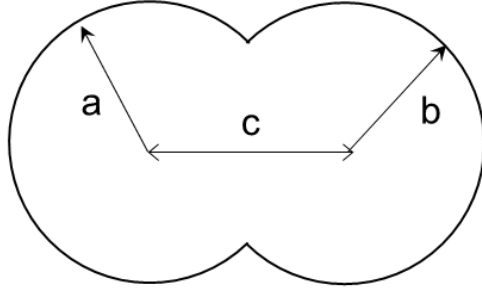


Figure 3: A cartoon of a dicolloidal particle. Radii of the two component spheres forming the dicolloid are a and b , while the distance between the centers of the two component spheres is c . In the present work only symmetric dicolloids with $a = b$ are considered.

particularly in concentrated suspensions, it is the lubrication interactions that dominate the overall particle-particle interactions. These considerations lead us to the development of the Fast Lubrication Dynamics technique (FLD), which is described below in the case of suspensions of spheres; its extension to anisotropic dicolloidal particles is presented later in Sec. (2.1.1).

In the FLD approach, the overall resistance tensor is approximated as^{20,21}

$$\mathbf{R} = \mathbf{R}_0 + \mathbf{R}_\delta, \quad (6)$$

where \mathbf{R}_δ is based on the near-field lubrication interactions summed pairwise^{21,24}, while a novel isotropic term \mathbf{R}_0 (diagonal tensor, function of volume fraction alone) is selected to match the mean particle mobility (equivalently the short time self-diffusivity) from the more detailed Stokesian Dynamics technique for spheres^{20,21}. Somewhat related approaches have been described before in the literature by Ball and Melrose²⁴ and by Banchio and Brady²⁵. The FLD approach has been shown to produce results comparable to the Stokesian Dynamics technique, while requiring only a fraction of the latter's cost; see Kumar²¹ and Kumar and Higdon²⁰ for details; further validation is provided in the recent work of Schunk et al.²⁶. We discuss next the extension of the FLD technique for modeling hydrodynamic interactions in dicolloidal particle suspensions.

2.1.1 FLD technique for dicolloidal Particles

In the FLD technique for dicolloidal particles (Fig. 3 shows a generic dicolloidal particle), the overall resistance tensor \mathbf{R} is expressed by an equation similar to Eq. (6). For simplicity, in the present effort, we take the value of \mathbf{R}_0 in a suspension of dicolloids to be the same as in a suspension of spheres at the same volume fraction, irrespective of the exact shape of the particle under consideration. For particles with small degree of anisotropy this is a

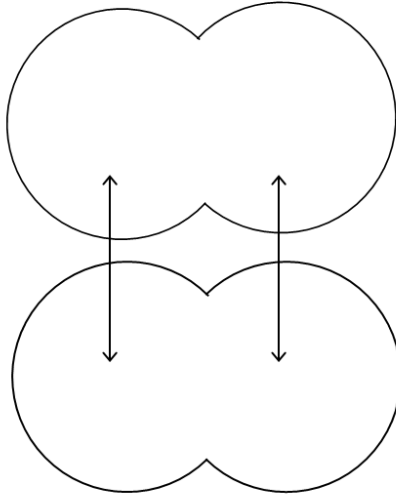


Figure 4: A cartoon showing two pairwise interactions between spherical components forming the two dicolloids.

fair assumption, though some error in the value of \mathbf{R}_0 can be expected at larger degree of anisotropy. Note that the largest aspect ratio particle investigated in the current work is $AR = 1.5$. Additionally, since our interest is only in concentrated suspensions with volume fraction $\phi \geq 0.3$, we estimate the contribution from this error to be small, as the hydrodynamic interactions will be dominated by the strong lubrication forces at these high volume fractions.

There are some additional considerations with the present choice of \mathbf{R}_0 , which deserve a brief comment. The tensor \mathbf{R}_0 in some ways represents the effective one-body resistance in the suspension. Our choice of \mathbf{R}_0 as an isotropic diagonal tensor implies that a dicolloidal particle, in the absence of interactions with other particles, will behave just like a sphere. For example, if we study an isolated dicolloidal particle with the current implementation of the FLD algorithm, then the dicolloid will not exhibit preferred flow alignment as might be expected for an anisotropic particle^{10,9}. However, this is not a great concern here as the particle dynamics, including its orientation behavior, will be dominated by the lubrication interactions at the volume fractions considered here.

Next, we discuss the computation of the near field lubrication term \mathbf{R}_δ in suspensions of dicolloidal particles. As shown in Fig. (3), a dicolloidal particle consists of two fused spheres (only symmetric dicolloids with $a = b$ are considered here). Given this fact, the lubrication interaction between two dicolloids can be modeled as a pairwise sum of one or more interactions between the constituent spheres forming the two dicolloids; this is schematically shown in Fig. (4) and discussed in detail elsewhere^{23,21}. Further note that up to four spherical node pairs can be formed between two dicolloidal particles, . In our algorithm, we do not necessarily consider all the four pairs. The selection of a spherical node pair for the lubrication calculation depends on two factors. First involves the satisfaction of a cut-off separation requirement – only those

spherical nodes pairs are considered in the lubrication calculation which have a center to center separation less than $2.5a$, where a is the radius of the spherical node. Second factor involves the concept of inter-visibility – only those spherical node pairs are considered for the lubrication calculation which are inter-visible. Mathematically, if the line joining the centers of the two spherical nodes passes through each of their surfaces, then that pair has inter-visibility and is considered for the lubrication calculation; otherwise it is rejected. This scheme essentially prevents double counting which can happen otherwise. We remark that similar procedures are used extensively in the literature for computing interparticle interactions between patchy particles – a popular example is the Kern-Frenkel model²⁷.

2.2 Brownian Force (\mathbf{F}^B)

Brownian forces and torques can be obtained from the fluctuation dissipation theorem and the equipartition of energy²⁸, which dictates

$$\langle \mathbf{F}^B \rangle = 0 \quad (7a)$$

$$\langle \mathbf{F}^B \mathbf{F}^B \rangle = 2kT \mathbf{R}_{FU} / \Delta t \quad (7b)$$

where $\langle \rangle$ denotes an ensemble average, \mathbf{R}_{FU} denotes the component of the resistance tensor representing generalized force-velocity coupling, while Δt , k and T denote the time step employed in the algorithm, the Boltzmann constant, and the system temperature respectively^{29,24,20}. Brownian forces/torques satisfying the above equations are easily obtained by employing uncorrelated random numbers with zero mean and unit variance. Briefly, we begin by writing the Brownian force/torque vector \mathbf{F}^B as

$$\mathbf{F}^B = \sqrt{\frac{2kT}{\Delta t}} (\mathbf{A}\boldsymbol{\alpha} + \mathbf{B}\boldsymbol{\beta}), \quad (8)$$

where $\boldsymbol{\alpha}$ and $\boldsymbol{\beta}$ are $6N_p$ vectors whose elements are uncorrelated random numbers, say γ_i , satisfying the aforementioned properties, namely

$$\langle \gamma_i \rangle = 0, \quad (9a)$$

$$\langle \gamma_i \gamma_j \rangle = \delta_{ij}, \quad (9b)$$

where δ_{ij} is the Kronecker delta function. With the random numbers satisfying the above properties, we only need to satisfy the following two equations to obtain the agreement of Eq. (8) with Eq. (7)

$$\begin{aligned} \mathbf{A}\mathbf{A}^T &= \mathbf{R}_0^{FU} \\ \mathbf{B}\mathbf{B}^T &= \mathbf{R}_\delta^{FU} \end{aligned} \quad (10)$$

The above equations require one to compute the square root of the matrices \mathbf{R}_0^{FU} and \mathbf{R}_δ^{FU} . In the present algorithm these are easily obtained as \mathbf{R}_0^{FU} is a diagonal matrix, while contributions from \mathbf{R}_δ^{FU} matrix can be summed pairwise. Details can be found in^{24,21}.

2.3 Repulsive Force \mathbf{F}^P

During time stepping, due to integration errors, particle overlaps can occur. To overcome this, we employ a short range repulsive force \mathbf{F}^P between the spherical node pairs as follows⁹:

$$\mathbf{F}^P = \begin{cases} C_p \left(\frac{\delta_{min}}{\delta} \right) \left(\eta - \frac{1}{2}\eta^2 \right)^3 \mathbf{d} & \text{if } \delta < \delta_{min} \\ 0 & \text{if } \delta > \delta_{min} \end{cases}, \quad (11)$$

where δ is the gap between the two spherical nodes, $\eta = 1 - \delta/\delta_{min}$, \mathbf{d} is the unit vector pointing from one spherical node to the other, and C_p is a parameter described below. In this work, the range of the repulsive force δ_{min} was fixed at $10^{-3}a$. For gaps smaller than a specified numerical tolerance, δ_{num} , both the hydrodynamic force and interparticle force are capped by evaluating at δ_{num} . This tolerance for all simulations presented here was set at $\delta_{num} = 10^{-5}a$. The interparticle force between a pair of dicolloids was computed as the sum of pairwise forces between the spherical nodes comprising the particles. The above form of the repulsive force gives a near hard sphere behavior with nonzero repulsive interaction only when the gap between a spherical node pair becomes less than $10^{-3}a$.

2.4 Solution procedure

The goal of the overall solution procedure is to compute the unknown particle velocities and angular velocities for a given set of Brownian forces, interparticle forces, and the imposed bulk (shear) flow. The unknown particle velocities/angular velocities can be obtained from the solution of the governing equation (3) written as:

$$\mathbf{R}_{FU} \cdot (\mathbf{U}^\infty - \mathbf{U}) = -(\mathbf{F}^P + \mathbf{F}^B) - \mathbf{R}_{FE} \cdot \mathbf{E}^\infty. \quad (12)$$

The above equation is obtained from Eq. (3) by replacing \mathbf{F}^H with its equivalent expressed in terms of the force-velocity (\mathbf{R}_{FU}) and force-rate of strain (\mathbf{R}_{FE}) couplings. In the present effort, we solve Eq. (12) iteratively with the conjugate gradient algorithm³⁰, which is applicable here owing to the symmetry and positive definiteness of the resistance coupling \mathbf{R}_{FU} . Once the particle velocities and angular velocities have been computed, the particle positions and orientations are evolved in time with a third order explicit Runge-Kutta method. The choices of the time-step Δt employed in the time integration step as well as the total time of integration t are discussed below. It is relevant to note here that all simulations in the present effort were initiated with a random configuration generated by a Monte Carlo method. A

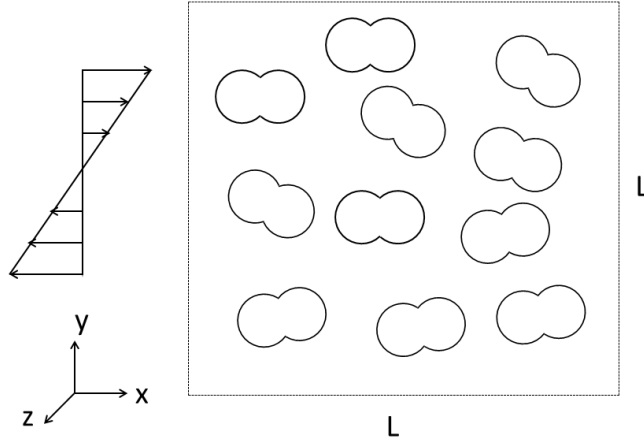


Figure 5: Schematic of the system geometry: a cubic simulation box (side L) with $N_p = 1000$ particles subjected to a simple shear flow is considered. Periodic boundary conditions are employed in all three directions.

Monte Carlo simulation for dicolloidal particles involved a random displacement to both the particle's orientation as well as its center of mass at each step, and this was continued until an apparent steady state was attained.

2.5 Simulation Parameters

In this section, we discuss some of important physical as well as numerical parameters in the current study. Perhaps the most important parameter in the present effort is the shear rate $\dot{\gamma}$, which is expressed in terms of the non-dimensional Péclet number (Pe). Note that the Péclet number gives the ratio of the diffusive and the convective time scales, and is defined in the present effort as:

$$Pe = \frac{\dot{\gamma}a^2}{D_0}, \quad (13)$$

where a is the radius of the spherical node forming the dicolloid, and $D_0 = kT/6\pi\mu a$ is the Stokes-Einstein diffusivity based on the radius of the spherical node. Alternative definitions of Pe based on length scales other than a is possible, though that will not change the value of Pe appreciably given the small degree of anisotropy of dicolloids. In the current effort, Pe was varied between $0 \leq Pe \leq 1000$. Another important parameter in the current study is the particle volume fraction ϕ , which was varied in the range $0.3 \leq \phi \leq 0.5$. Lastly, in the context of the present work, two particle shape parameters are required for defining a dicolloid. The two shape parameters are the ratio of the radii of the component spheres, b/a , and the ratio of the center to center distance and one of the radius, c/a ; see Fig. (3) illustrating a generic dicolloidal particle. In the present study, we have investigated two different dicolloidal particles named as homonuclear and fused-dumbbell particles (Fig. 2). The shape parameters ($b/a, c/a$) for these two particle shapes are (1,0.2) for homonuclear particles and (1,1) for fused-

dumbbells. The geometric aspect ratio for these particles can be obtained as $AR = (2a+c)/2a$, which yields $AR = 1.1$ for homonuclear particles and $AR = 1.5$ for fused-dumbbell particles.

There are several other parameters associated with the numerical solution procedure. First is the choice of the simulation box, which is taken to be cubic here with periodic boundary conditions employed in all three directions. A schematic of the system geometry is illustrated in Fig. (5). The number of particles in the simulation box was set to $N_p = 1000$. The next parameter is the non-dimensional time-step Δt^* , which varied in the range $10^{-3} - 10^{-4}$; typically, a lower Δt^* is required at high volume fractions or low shear rates. We note that the non-dimensionalization of the time-step depends on the shear rate (Pe). At low shear rates ($Pe < 1$), Δt is non-dimensionalized by the diffusive time scale, i.e., $\Delta t^* = D_0/a^2\Delta t$, while at higher shear rates ($Pe \geq 1$), Δt is non-dimensionalized by the convective time scale, i.e., $\Delta t^* = \dot{\gamma}\Delta t$. The total non-dimensional integration time t^* was $t^* = 500$, with t being non-dimensionalized in the same way as Δt . This total integration time was found to be sufficient to obtain good statistical averages of various properties in the apparent steady state – in most cases, an apparent steady state was evident for times greater than $t^* > 150$ as evidenced by various of the suspension properties, like the orientation distribution function. The last parameter of interest is the repulsive force prefactor C_p , which in the non-dimensional form is set to $C_p^* = 10$. At low shear rates ($Pe < 1$), C_p is non-dimensionalized as: $C_p^* = C_p/(8\pi\mu a^4/D_0)$, while at higher shear rates ($Pe \geq 1$), C_p is non-dimensionalization as: $C_p^* = C_p/(8\pi\mu a^2\dot{\gamma})$. The specification of various of the above parameters concludes the formulation section. We now turn our attention to the results from the numerical simulations, which are presented in the sections below.

3 Results and Discussion

3.1 Microstructure

In this section, we present results for the positional (center-of-mass) microstructure in suspensions of homonuclear and fused-dumbbell particles. Results are presented for volume fractions between $\phi = 0.3$ and $\phi = 0.5$ and for a wide range of Péclet numbers varying between $Pe = 0$ and $Pe = 1000$. Figure (6) shows some illustrative simulation snapshots at $Pe = 10$ for both the homonuclear and the fused-dumbbell particles in $\phi = 0.3$ and $\phi = 0.5$ suspensions. These snapshots are in the front view, i.e., in the velocity–gradient ($x - y$) plane. At the lower volume fraction of $\phi = 0.3$, there are no signs of ordering for both the particle shapes. At the higher volume fraction of $\phi = 0.5$, several regions with a string like structure aligned in the flow direction are apparent in the homonuclear particle suspension, though the fused-dumbbell particle suspension appears mostly disordered even at this volume fraction.

For a more quantitative characterization of the microstructure, we will employ the commonly used measure of pair distribution function (PDF) denoted $g(x, y, z)$. Note that the PDF gives the conditional probability of finding a particle at a given location (x, y, z) pro-

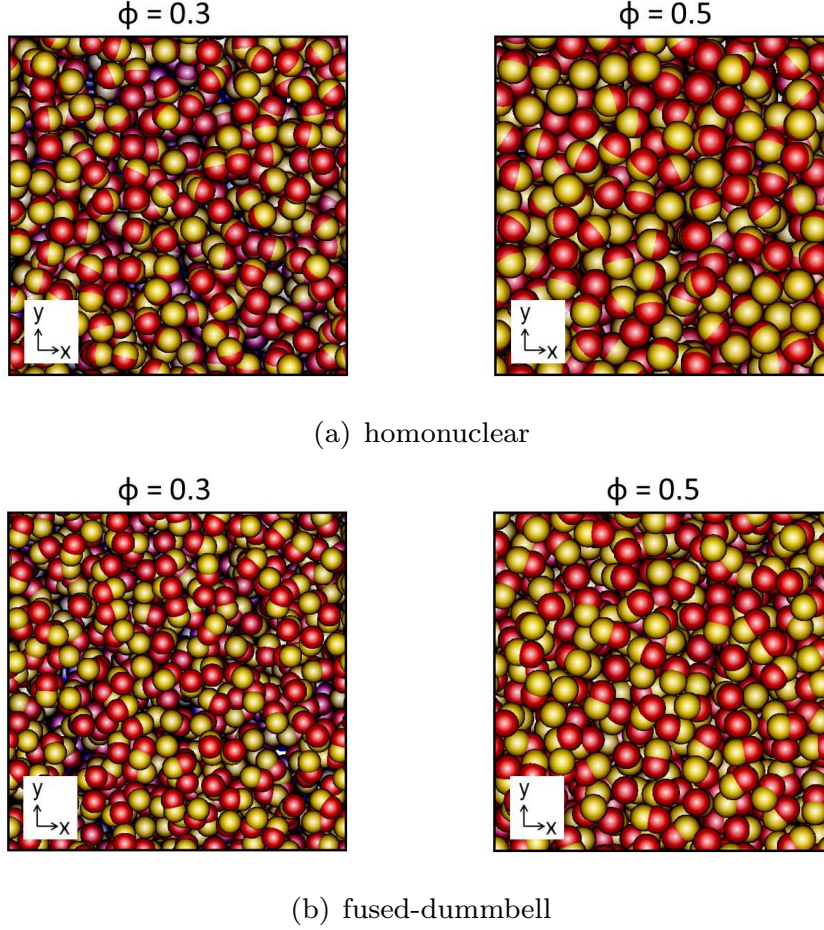


Figure 6: Simulation snapshots in the front view ($x - y$ plane) at a shear rate of $Pe = 10$ and for two different volume fractions ($\phi = 0.3$ and $\phi = 0.5$) for (a) homonuclear particles and (b) fused-dumbbell particles.

vided a particle is already present at the origin. Additionally, the PDFs are normalized such that $g(x, y, z) = 1$ in the absence of any correlations between particle positions. Given the full three dimensional PDF $g(x, y, z)$, it is usually instructive to consider its projections in various two dimensional planes – the projection in the front view ($x - y$ plane) denoted $g(x, y)$ will be of particular interest. Formally, $g(x, y)$ is defined as follows:

$$g(x, y) = \frac{1}{2a} \int_{-a}^{+a} g(x, y, z) dz. \quad (14)$$

The PDF in the front view for homonuclear particles in $\phi = 0.3$ and $\phi = 0.5$ suspensions are shown in Fig. (7) at several Péclet numbers between $Pe = 0$ and $Pe = 1000$; figure (8) illustrates the same for fused-dumbbell particle suspensions. It is appropriate to remark here that the color scheme used in the PDF plot is chosen to emphasize small differences from the value of one, and, as such, different patterns in these plots do not necessarily imply

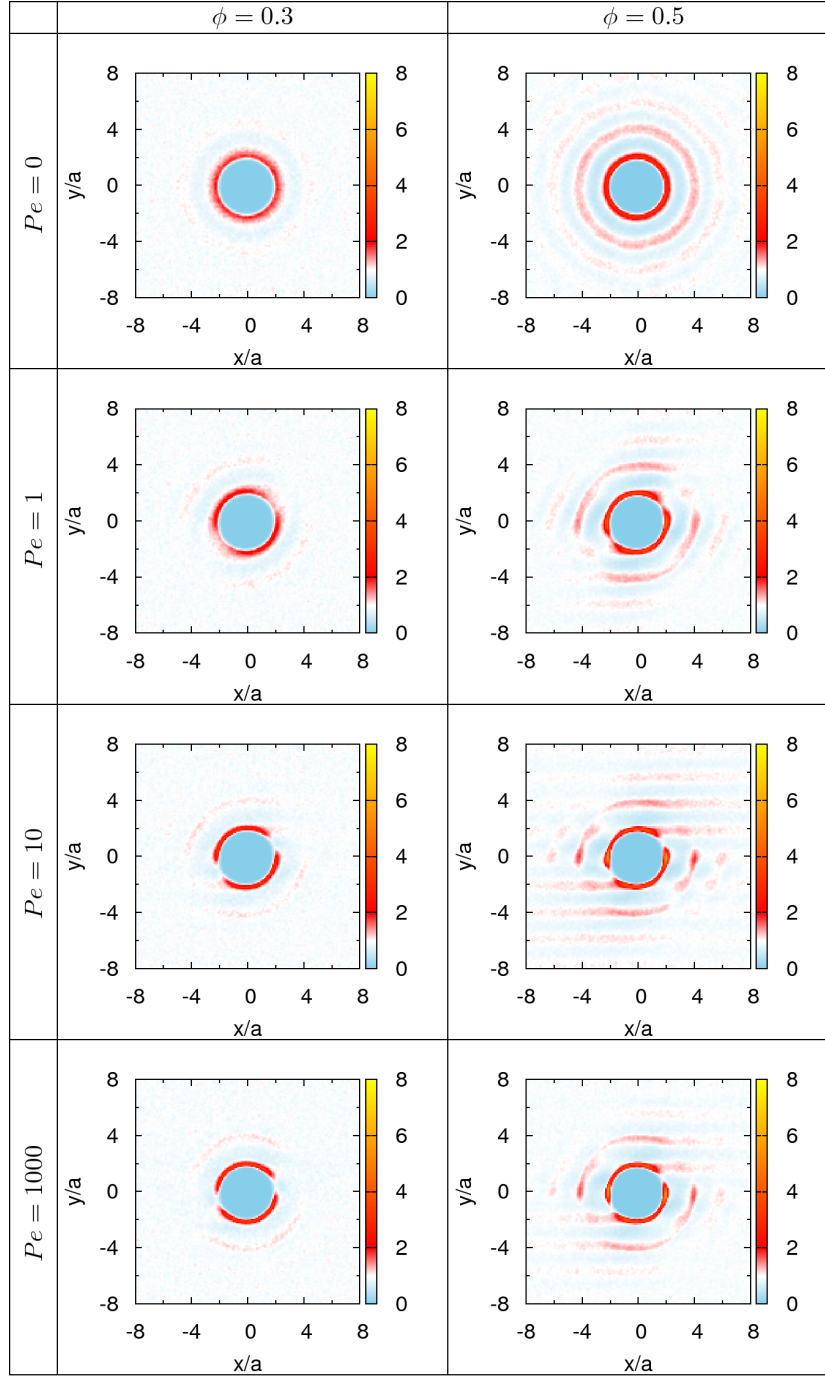


Figure 7: Pair distribution function in the front view ($x - y$ plane) for homonuclear particles at several Pe and two different volume fractions ($\phi = 0.3$ and $\phi = 0.5$).

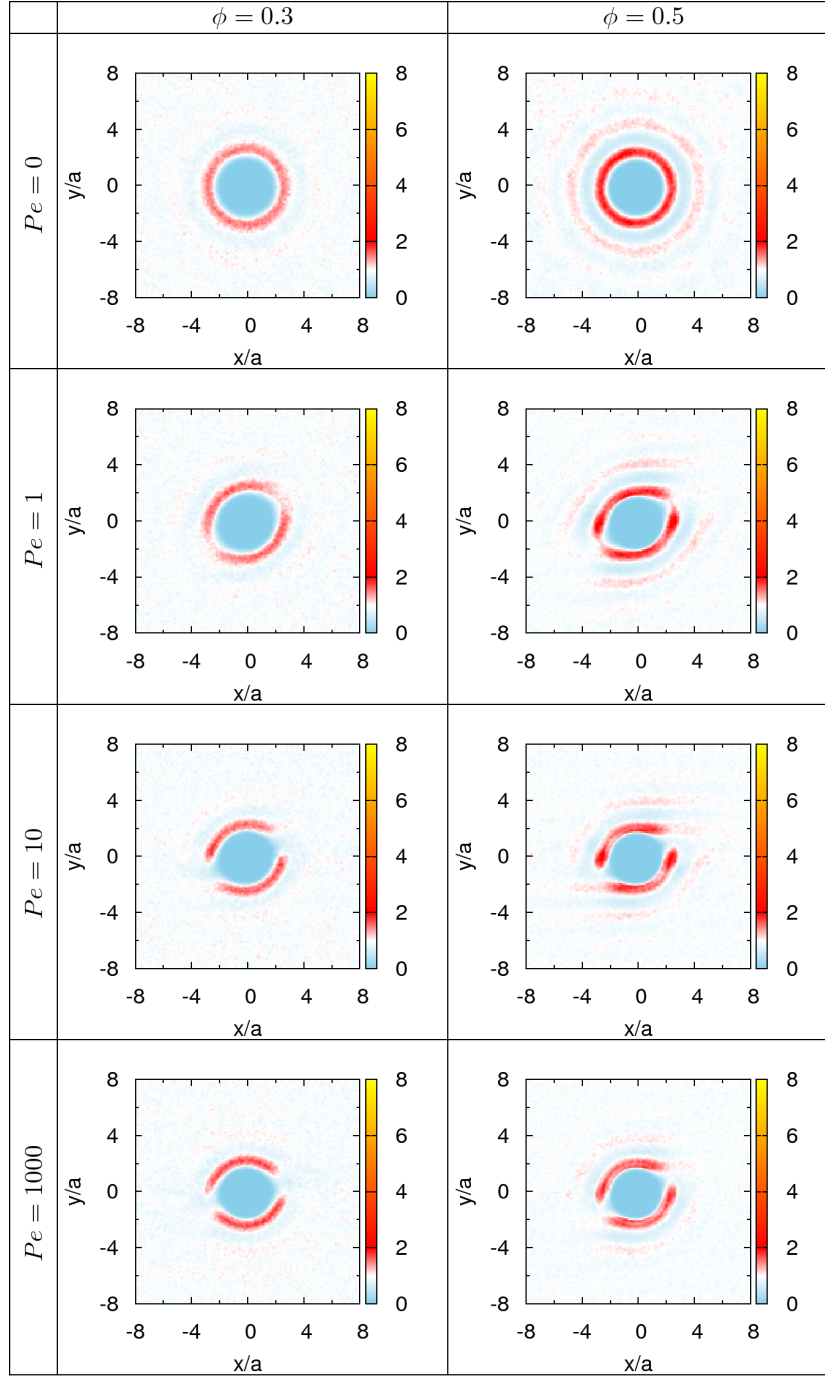


Figure 8: Pair distribution function in the front view ($x-y$ plane) for fused-dumbbell particles at several Pe and two different volume fractions ($\phi = 0.3$ and $\phi = 0.5$).

magnitudes greatly different from one. Returning to the above two figures (Figs. 7 and 8), we note that at equilibrium ($Pe = 0$), a disordered microstructure is apparent in suspensions of both the homonuclear and fused-dumbbell particles at $\phi = 0.3$; in these plots, only the first coordination shell distinctive of an amorphous fluid like structure is apparent. At the higher volume fraction of $\phi = 0.5$, the structure stays disordered at $Pe = 0$, though in these cases the second (for fused-dumbbell) or third (for homonuclear) coordination shells are also apparent. A disordered structure at equilibrium at these volume fractions is consistent with the Monte Carlo simulations of Vega et al.³¹. As per the previous reference, a suspension of homonuclear particles are in a fluid like state below a volume fraction of $\phi = 0.4945$ (called freezing point) and a crystalline solid state above $\phi = 0.543$ (called melting point); between these two volume fractions the two phases coexist. In fused-dumbbell particle suspensions, the freezing and melting transitions were found to occur at approximately $\phi = 0.6013$ and $\phi = 0.6463$. Typically, in simulations, the ordered phase is observed at volume fractions above the melting transition³². Therefore, a fluid like state is expected at equilibrium in suspensions of homonuclear as well as fused-dumbbell particles for volume fractions up to $\phi = 0.5$ considered here. It is interesting to remark here that the ordered phase at the freezing transition is orientationally disordered (plastic crystal) face centered cubic in suspensions of homonuclear particles, while it is orientationally ordered base centered monoclinic in fused-dumbbell particle suspensions³¹. It is also pertinent to remark here that a nematic phase is not expected in dicolloidal particle suspensions. This is due to the fact that the degree of anisotropy of dicolloids is small, while the nematic phase is stable only at higher aspect ratios. As an example, for spherocylinders, the nematic phase becomes stable at an aspect ratio of 4.7³³.

We next discuss the microstructure in the $\phi = 0.3$ suspensions of homonuclear and fused-dumbbell particles at finite rates of shear. At very low shear rates ($Pe = 0.01$), the microstructure is found to be very similar to the equilibrium microstructure in both the homonuclear and the fused-dumbbell particle suspensions (not shown). As the shear rate is further increased ($Pe = 1$ in the first column of Figs. 7 and 8), the microstructure becomes distorted – there is an enhancement in pair probability in the compressional quadrants, accompanied by its depletion in the extensional quadrants. This fore-aft asymmetry in the PDF results due to the presence of Brownian forces as discussed in Brady and Morris³⁴ and Foss and Brady²⁹. Lastly, we note that the microstructure remains disordered at the highest shear rates investigated here ($Pe = 1000$) in the $\phi = 0.3$ suspensions (Figs. 7 and 8).

At the higher volume fraction of $\phi = 0.5$, some interesting features emerge in the PDFs of both the particle shapes (Figs. 7 and 8). At low shear rates ($Pe = 0.01$), the microstructure is similar to the equilibrium microstructure for both the particle shapes (not shown). However, at $Pe = 10$, evidence of weak string like ordering is apparent in suspensions of homonuclear particles (horizontal bands in Fig. 7), which is sustained at higher shear rates, though the ordering become progressively weaker (e.g., compare PDF at $Pe = 10$ with PDF at $Pe =$

1000). In fused-dumbbell particle suspensions, the microstructure shows similar hints of string like ordering at $Pe = 10$, though the strength of ordering is considerably weaker than in suspensions of homonuclear particles (Fig. 8). At further higher shear rates in fused-dumbbell particle suspensions (e.g., $Pe = 1000$), the microstructure appears mostly disordered.

The results presented in the current study are consistent with previous experimental and computational efforts. In experimental studies on near hard sphere suspensions, Ackerson³⁵ noted that suspensions which are disordered (liquid-like) at rest stays disordered under shear. This is consistent with the disordered structure observed in $\phi = 0.3$ suspensions of homonuclear particles under shear, and also in fused-dumbbell particle suspensions for volume fractions up to $\phi = 0.5$ considered here. Ackerson³⁵ also noted that at volume fractions near the freezing transition, string like structures begin to coexist with amorphous fluid like regions at intermediate rates of shear – this is similar to the weak string like ordering observed in $\phi = 0.5$ homonuclear particle suspension. Similarly, in Stokesian Dynamics simulations on non-Brownian dicolloidal particle suspensions, which is equivalent to the high Pe limit, Kumar and Higdon⁹ also observed weak string like ordering in suspensions of homonuclear particles at $\phi = 0.5$. In independent Stokesian dynamics simulations of Sierou and Brady¹⁸, again for non-Brownian particles, very strong string like ordering was observed in suspensions of spheres at $\phi = 0.52$, which is just above the freezing point of $\phi = 0.494$ in hard sphere suspensions. It is instructive to note that in suspensions that are ordered at rest, like in sufficiently charged particle suspensions, very distinct and rich set of microstructural transitions are observed as a function of shear rate; see, e.g., Chen et al.³⁶, Chow and Zukoski³⁷. This regime, however, is not relevant to our study here. Finally, there have been very limited experimental studies on the microstructure of dicolloidal particle suspensions under steady shear. The only study we are aware of is that by Mock and Zukoski³⁸, who studied *charge-stabilized* dicolloidal particle suspensions under shear at a volume fraction of $\phi = 0.42$. The homonuclear particle equivalent investigated in this work was found to possess a polycrystalline structure at rest, a sliding layer structure at intermediate rates of shear, and an amorphous structure at further higher shear rates. A direct comparison of this work with the present effort, though, is not possible due to the presence of strong electrostatic repulsion in the former study.

3.2 Orientation behavior

We next present the results on the orientation behavior in homonuclear and fused-dumbbell particle suspensions as a function of Pe for volume fractions between $\phi = 0.3$ and $\phi = 0.5$. The statistical distribution of the particle orientation will be characterized by the orientation distribution function (ODF) denoted $P(\theta, \varphi)$, where θ and φ are spherical coordinates as illustrated in Fig. (2); also see Fig. (10) for illustrations of the angle φ . In words, θ is the polar angle between the director \mathbf{n} of the particle and the z-axis, while φ is the azimuthal angle between its projection in the $x - y$ plane and the y -axis measured clockwise. Based on the ODF $P(\theta, \varphi)$, the differential probability of finding a particle with an orientation between

$(\theta, \theta+d\theta)$ and $(\varphi, \varphi+d\varphi)$, dN , can be expressed as follows:

$$dN = \frac{1}{4\pi} P(\theta, \varphi) \sin \theta d\theta d\varphi. \quad (15)$$

Additionally, we note that the $P(\theta, \varphi)$ satisfies the following normalization constraint:

$$\int_{-\pi/2}^{\pi/2} \int_0^{\pi/2} P(\theta, \varphi) \sin \theta d\theta d\varphi = 1, \quad (16)$$

where we have restricted the limits of integration in θ to $[0, \pi/2]$ and in φ to $[-\pi/2, \pi/2]$, which is half of the corresponding overall ranges; this is sufficient here owing to the symmetry of the ODF $P(\theta, \varphi)$. We next introduce one dimensional ODFs, $P(\theta)$ and $P(\varphi)$, which are defined as follows:

$$P(\theta) = \int_{-\pi/2}^{\pi/2} P(\theta, \varphi) d\varphi, \quad (17a)$$

$$P(\varphi) = \pi \int_0^{\pi/2} P(\theta, \varphi) \sin \theta d\theta. \quad (17b)$$

We will use $P(\theta)$ and $P(\varphi)$ extensively in lieu of the full ODF $P(\theta, \varphi)$. It is important to emphasize here that the definitions of $P(\theta)$ and $P(\varphi)$ are such that a uniform distribution in the orientation space will result in $P(\theta) = 1$ and $P(\varphi) = 1$. For later use, we also define a suspension averaged θ and φ , denoted θ_m and φ_m , as follows:

$$\theta_m = \int_0^{\pi/2} \theta P(\theta) \sin \theta d\theta, \quad (18a)$$

$$\varphi_m = \frac{1}{\pi} \int_{-\pi/2}^{\pi/2} |\varphi| P(\varphi) d\varphi. \quad (18b)$$

Note the absolute value term ‘ $|\varphi|$ ’ in the definition of φ_m above. A simple interpretation of θ_m is that it gives the mean inclination of the particle director with the z axis. Similarly, φ_m gives the mean inclination of the projection of the particle director in the $x - y$ plane with the y axis. As should be obvious from the above definitions, θ_m and φ_m have the following bounds: $0 \leq \theta_m \leq \pi/2$ and $0 \leq \varphi_m \leq \pi/2$. In a suspension with a completely random orientation distribution, these two averages will be denoted by θ_m^0 and φ_m^0 . We then define $\Delta\theta_m$ and $\Delta\varphi_m$ for an arbitrary suspension as follows:

$$\Delta\theta_m = \theta_m - \theta_m^0, \quad (19a)$$

$$\Delta\varphi_m = \varphi_m - \varphi_m^0. \quad (19b)$$

When $\Delta\theta_m$ is negative, it will imply an enhanced vorticity alignment in comparison to an isotropic distribution, while positive $\Delta\theta_m$ will imply an enhanced alignment in the velocity-gradient plane (i.e., away from the vorticity axis) in comparison to an isotropic distribution. A

positive $\Delta\varphi_m$ will imply an enhanced alignment with the velocity axis in the velocity–gradient plane, while a negative $\Delta\varphi_m$ will imply an enhanced alignment with the gradient axis in the velocity–gradient plane, both, of course, are relative to an isotropic distribution.

In addition to the above measures, it will be useful to employ direct measures of the particle orientation relative to the three coordinate axes x , y , and z . In the present work, this measure is provided by the orientation order parameter S_{ii} defined relative to the axis i , where i could be x , y , or z . More specifically, the orientational order parameter S_{ii} is defined as the average over all particles of

$$S_{ii} = \frac{3}{2}n_i n_i - \frac{1}{2}. \quad (20)$$

Some representative values of S_{ii} are as follows. For a random orientation distribution $S_{ii} = 0$; for perfect alignment of particles with axis i , $S_{ii} = 1.0$; and for particles aligned in the plane perpendicular to axis i , $S_{ii} = -0.5$. It is evident from the above definition that an increased degree of particle alignment with an axis i will result in a higher value of S_{ii} .

Having introduced the various measures for characterizing the orientation behavior, we turn our attention to the results for these measures. We will first present the orientation distribution in the θ coordinate as a function of Pe , volume fraction and particle shapes in Sec. (3.2.1). Following this, we will present the orientation distribution in φ coordinate in Sec. (3.2.2). Lastly, we will present the results for the orientation order parameters in Sec. (3.2.3).

3.2.1 Orientation distribution in θ coordinate

Figures (9a) and (9b) show the orientation distribution function $P(\theta)$ at several Péclet numbers in homonuclear particle suspensions with $\phi = 0.3$ and $\phi = 0.5$, respectively. The same two plots for suspensions of fused-dumbbell particles are shown in Figs. (9d) and (9e), respectively. The change in the suspension averaged θ over an isotropic distribution, $\Delta\theta_m$, is shown in Fig. (9c) for homonuclear particle suspensions, while it is shown in Fig. (9f) for fused-dumbbell particle suspensions.

We first consider the orientation behavior in suspensions of homonuclear particles. At low shear rates ($Pe = 0.01$) in the $\phi = 0.3$ suspension, $P(\theta)$ has a value close to one, implying a random distribution in θ at these shear rates (Fig. 9a). As the shear rate is further increased, an enhancement in probability at low θ values is observed, indicating an increased vorticity alignment; this enhancement is particularly strong at $Pe = 1000$ (Fig. 9a). We see a very similar trend at the higher volume fraction of $\phi = 0.5$ (Fig. 9b), namely, a random distribution in θ at low shear rates ($Pe = 0.01$), which shifts towards lower θ values, i.e., increased vorticity alignment, at higher shear rates (e.g. $Pe = 1000$). These trends in the orientation behavior with shear rate are also evident in the plot of $\Delta\theta_m$ in Fig. (9c). At low shear rates, $\Delta\theta_m$ is nearly zero indicating a random orientation distribution, while it becomes progressively more

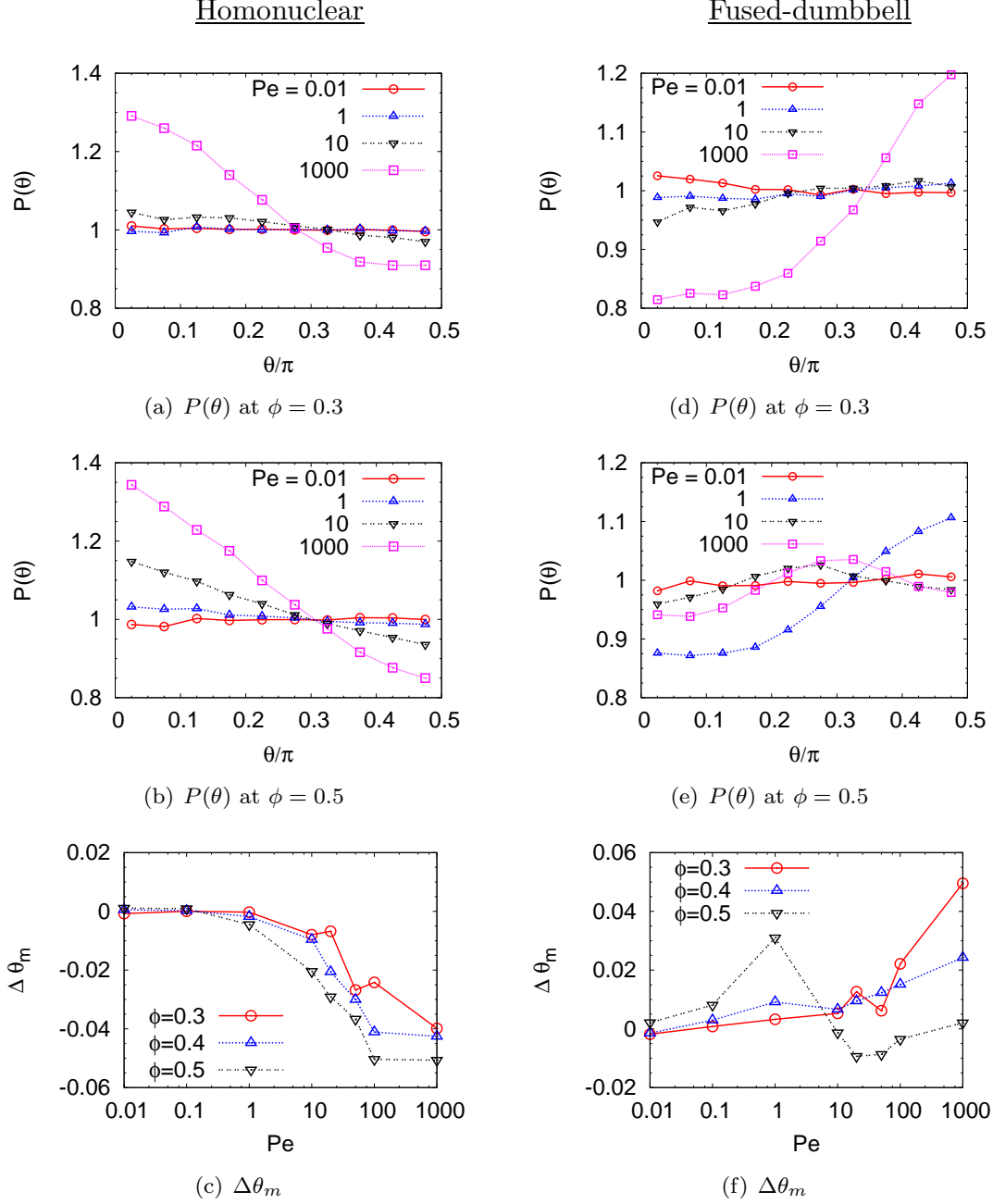


Figure 9: $P(\theta)$ and $\Delta\theta_m$ for (a), (b), and (c) homonuclear particles and (d), (e) and (f) fused-dumbbell particles.

negative with increasing shear rates, implying an increased vorticity alignment at higher shear rates. It is also evident in the plot that $\Delta\theta_m$ is more negative at higher volume fractions, implying a greater vorticity alignment at higher volume fractions in homonuclear particle suspensions.

We next discuss the orientation results in suspensions of fused-dumbbell particles. Focusing on the plot of $P(\theta)$ in $\phi = 0.3$ fused-dumbbell particle suspension (Fig. 9d), it is obvious that

the distribution at low shear rates ($Pe = 0.01$) is close to random. With increasing shear rates, however, $P(\theta)$ changes from a random distribution to a distribution skewed towards higher θ values, indicating an enhanced alignment in the velocity–gradient plane (Fig. 9d). This trend is clearly opposite to the trend observed in homonuclear particle suspensions. At the higher volume fraction ($\phi = 0.5$), the behavior is more complex (Fig. 9e). In this case, at intermediate shear rates ($Pe = 1$), an enhanced alignment in the velocity–gradient plane (i.e., at θ values) is observed. With further increase in shear rate, however, the enhanced particle alignment in the velocity–gradient plane is attenuated (e.g., at $Pe = 1000$), and the distribution gradually shifts towards vorticity alignment, though it is not as complete or as strong as in homonuclear particle suspensions. We confirm these observations by examining the plot of $\Delta\theta_m$ in Fig. (9f). It is evident from the figure that, at low volume fractions ($\phi = 0.3$), $\Delta\theta_m$ increases nearly monotonically with increasing shear rate, indicating an increasing alignment in the velocity–gradient plane. However, at $\phi = 0.5$, $\Delta\theta_m$ initially increases with increasing shear rate till $Pe = 1$, and thereafter it decreases and becomes negative with increasing shear rates before settling at a near zero value.

In a recent study⁹, we investigated the orientation distribution in the θ coordinate in sheared non-Brownian suspensions of dicolloids. More precisely, the orientation distribution into Jeffery’s orbits was investigated, which approximately corresponds to a distribution in the θ coordinate for small aspect ratio particles like dicolloids. This study indicates that in low volume fraction suspensions, both the homonuclear and fused-dumbbell particles exhibit increased particle alignment in the velocity–gradient plane. The increase in the velocity–gradient alignment in suspensions of fused-dumbbell particles was found to be considerably higher than in the suspensions of homonuclear particles. At higher volume fractions, both the particle shapes were found to exhibit a shift towards enhanced vorticity alignment, though the degree of vorticity alignment was much weaker in suspensions of fused-dumbbells than in suspensions of homonuclear particles. The origins of the contrasting behavior at low and high volume fractions was attributed to two different mechanisms at play in these two parameter regimes. At low volume fractions, on an average, it was observed that a particle aligned with the vorticity axis underwent comparatively stronger fluctuation in its orientation during the course of a collision with another particle. This behavior leads to non-uniform fluctuations in the orientation space with a stronger fluctuation observed for vorticity aligned particles. Additionally, the non-uniformity of fluctuations was found to be stronger and distributed over a wider region in the orientation space for the more anisotropic fused-dumbbell particles than the homonuclear particles. As discussed in Shaqfeh and Koch¹⁷, these non-uniform fluctuations will result in a drift away from regions of higher fluctuations towards regions of lower fluctuations. Predictions based on this mechanism easily resolves two of the key observations at low volume fractions, namely, an increased alignment in the velocity–gradient plane in both the homonuclear and the fused-dumbbell particle suspensions, and a comparatively greater alignment in the velocity–gradient plane in fused-dumbbell particle suspensions. At higher

volume fractions, the fluctuations were found to be nearly uniform in the orientation space and hence cannot lead to a non-uniform orientation distribution. The high volume fraction behavior was instead found to be driven by the negative second normal stress difference exhibited by these suspensions at high volume fractions (note that at low volume fractions, the normal stress differences are very weak). A detailed discussion of this mechanism is beyond the scope of the current work and the interested reader is referred to the original publication⁹. The greater vorticity alignment of the homonuclear particles than that of the fused-dumbbell particles at high volume fractions was shown to result from the lower degree of anisotropy of homonuclear particles. In essence this implies that the homonuclear particles have a greater rotational “mobility” than fused-dumbbell particles in concentrated suspensions, and hence the second normal stress difference is a more effective driving force in the former case.

With the aid of the above discussion, we can provide some mechanistic insights into the observed orientation behavior in the current study. Firstly, in all cases, a random orientation at low shear rates is expected due to the dominant effect of the Brownian forces in this regime. The high shear rate regime is well explained by the non-Brownian limit discussed above. The non-Brownian limit consistently explains the enhanced vorticity alignment observed in suspensions of homonuclear particles at high shear rates and at all volume fractions considered here. It also consistently explains the enhanced velocity-gradient plane alignment in low volume fraction suspensions of fused-dumbbell particles, and the (weak) vorticity alignment in higher volume fraction suspensions of fused-dumbbell particles, both in the high shear rate limit. The only regime that remains to be resolved is the intermediate shear rate regime. Intuitively, one may expect that the behavior at intermediate shear rates will be “intermediate” of the high and the low shear rate behaviors. This is certainly found to be true, but there is one exception – the intermediate shear rate behavior in the $\phi = 0.5$ fused-dumbbell particle suspension (Fig. 9f). In this case a random distribution is observed at low shear rates, while a weak vorticity alignment is observed at higher shear rate. The intermediate shear rate, however, exhibits enhanced velocity-gradient alignment. The origins of this behavior is not entirely clear, though it is possible that the “non-uniform fluctuation” mechanism plays a role at intermediate shear rates in high volume fraction suspensions as well (at very low shear rates Brownian motion will dominate any other effect). Further studies are clearly necessary to confirm this mechanism.

3.2.2 Orientation distribution in φ coordinate

The orientation distribution in the φ coordinate will be characterized by the ODF $P(\varphi)$ as well as by $\Delta\varphi_m$, the change in the suspension averaged φ in comparison to an isotropic distribution. For homonuclear particles, Fig. (11a) shows $P(\varphi)$ in $\phi = 0.3$ suspension and Fig. (11b) shows the same in $\phi = 0.5$ suspension; the plot for $\Delta\varphi_m$ is shown in Fig. (11c). For fused-dumbbell particles, Fig. (11d) shows $P(\varphi)$ in $\phi = 0.3$ suspension and Fig. (11e) shows the same in $\phi = 0.5$ suspension; the plot for $\Delta\varphi_m$ is shown in Fig. (11f).

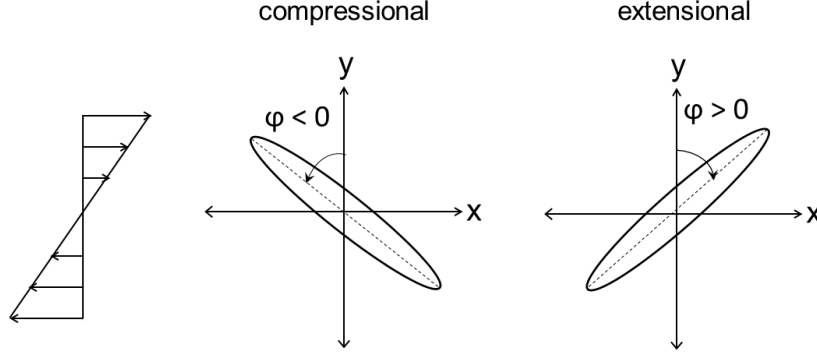


Figure 10: Examples of particles aligned in the compressional and the extensional quadrants.

We begin our discussion by examining the ODF $P(\varphi)$ in homonuclear particle suspensions at $\phi = 0.3$ (Fig. 11a). At low shear rates ($Pe = 0.01$), a random distribution is obvious as $P(\varphi) \approx 1$. At intermediate rates of shear ($Pe = 1$) for the same suspension, we find a decrease in probability corresponding to orientations in the compressional quadrant ($-0.5 < \varphi/\pi < 0$) accompanied by an increase in probability corresponding to orientations in the extensional quadrant ($0 < \varphi/\pi < 0.5$). Examples of particles aligned in the compressional and extensional quadrants are illustrated in Fig. (10). At higher shear rates (e.g., $Pe = 1000$ in Fig. 11a), the height of probability maxima as well as the depth of probability minima increases. Additionally, the probability minima is found to shift closer to the gradient axis ($\varphi = 0$) and the probability maxima closer to the velocity axis ($\varphi = \pi/2$) with increasing shear rates (e.g., compare $Pe = 1$ and $Pe = 1000$ in Fig. 11a). Turning our attention to suspensions of fused-dumbbell particles at the same volume fraction ($\phi = 0.3$), we observe the same trends in the ODF $P(\varphi)$ as in the suspension of homonuclear particles (compare Fig. 11a and 11d).

At the higher volume fraction of $\phi = 0.5$, the ODF $P(\varphi)$ shows additional features in both the homonuclear and the fused-dumbbell particle suspensions (Figs. 11b and 11e). In the homonuclear particle suspension, an expected random distribution is evident at $Pe = 0.01$ (Fig. 11b). At intermediate shear rates ($Pe = 1$), similar to the $\phi = 0.3$ suspension, an enhancement in probability corresponding to orientations in the extensional quadrant and a reduction in probability corresponding to orientations in the compressional quadrant is observed (Fig. 11b). However, with further increase in shear rate ($Pe = 10$), the height of the probability maxima as well as the depth of the probability minima decreases (Fig. 11b). This is in contrast to the behavior at low volume fractions discussed above. This trend at $Pe = 10$ is also evident in fused-dumbbell particle suspensions at this volume fraction (Fig. 11e). At further higher shear rates (e.g., $Pe = 1000$), the height of the maxima as well as the depth of the minima generally increases in suspensions of the homonuclear particles (Fig. 11b), but decreases slightly in suspensions of fused-dumbbell particles (Fig. 11e).

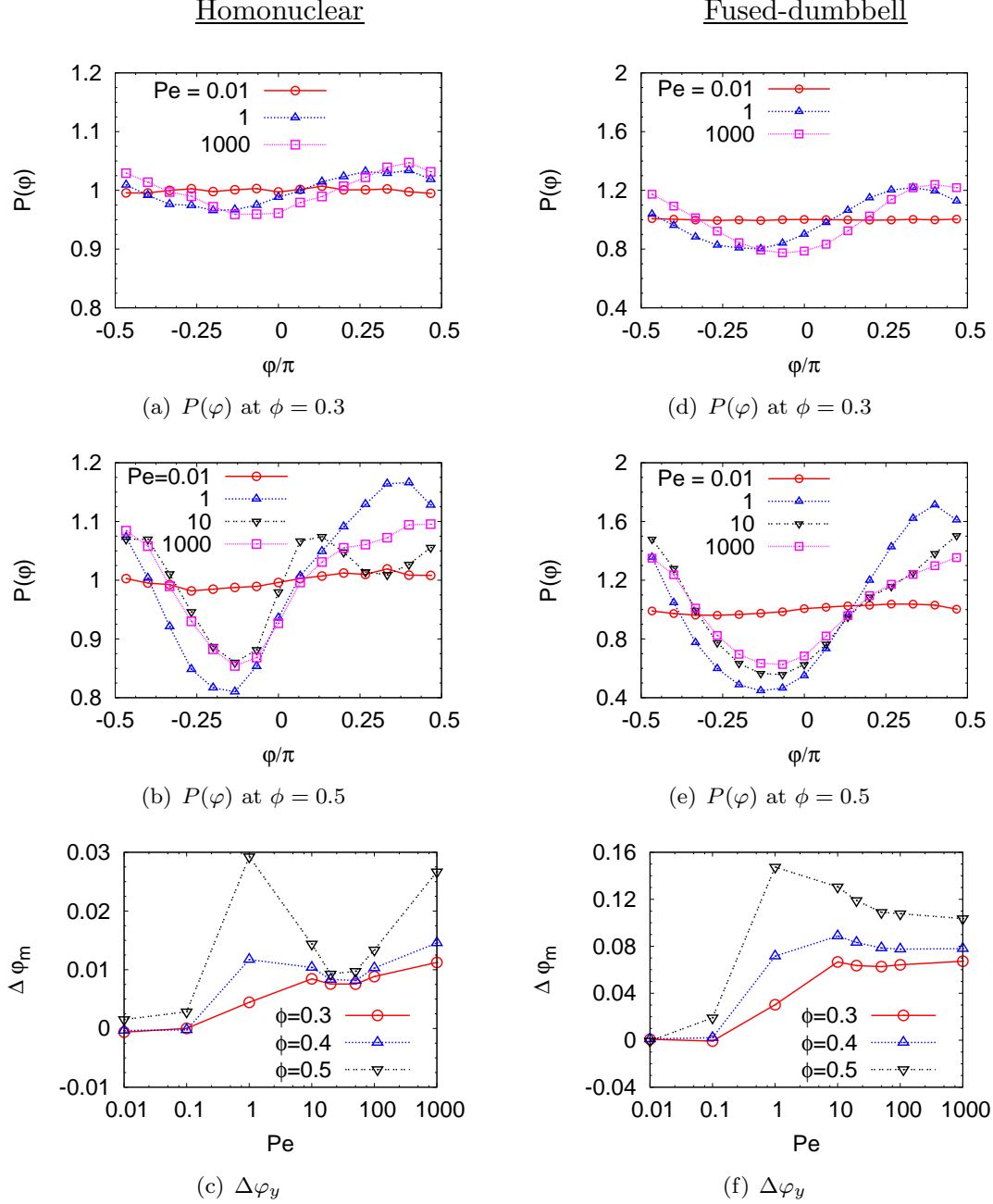


Figure 11: $P(\varphi)$ and $\Delta\varphi_m$ for (a), (b), and (c) homonuclear particles and (d), (e) and (f) fused-dumbbell particles.

The trends in the ODF $P(\varphi)$ discussed above are confirmed in the $\Delta\varphi_m$ plots shown in Fig. (11c) for homonuclear particles and in Fig. (11f) for fused-dumbbell particles. For both homonuclear and fused-dumbbell particles, there is a general tendency of increasing $\Delta\varphi_m$ with increasing volume fractions. Further, for both particle shapes, $\Delta\varphi_m$ increases with increasing shear rates at low volume fractions (e.g., $\phi = 0.3$). At high volume fractions, however, $\Delta\varphi_m$ does not necessarily increase with increasing shear rates. This is particularly evident in the

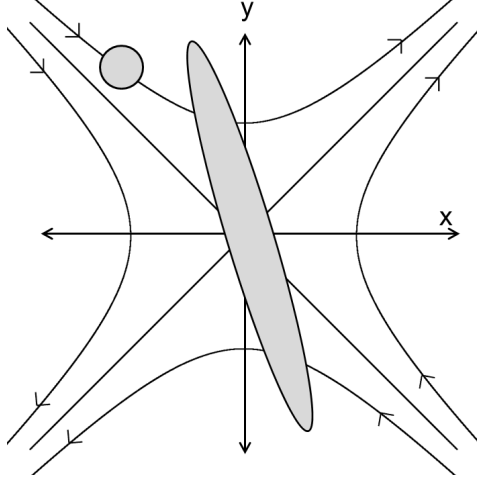


Figure 12: A cartoon showing a slender body subjected to an extensional flow. Also shown is a small sphere “colliding” with the slender body.

$\phi = 0.5$ homonuclear particle suspensions, where $\Delta\varphi_m$ is found to decrease in a small shear rate window around $Pe = 10$ (Fig. 11c). In fused-dumbbell suspensions at high volume fractions, $\Delta\varphi_m$ is found to decrease at all shear rates above $Pe > 1$ (Fig. 11f). Another feature apparent in the plots of $\Delta\varphi_m$ for the two particle shapes is that its magnitude is considerably larger in suspensions of fused-dumbbell particles than in suspensions of homonuclear particles. It is worth recalling at this point that $\Delta\varphi_m$ has important implications for results on the flow and the gradient alignment of the particle, e.g., a higher positive $\Delta\varphi_m$ will imply a greater degree of flow alignment at the expense of gradient alignment in the velocity–gradient plane. These aspects are discussed further in Sec. (3.2.3).

Some of the trends in the ODF $P(\varphi)$ as a function of shear rate have striking similarities with the corresponding trends in suspensions of Brownian axisymmetric particles at infinite dilution. We discussed the orientation behavior in such systems in the introduction and we summarize the key observations here. At equilibrium, the orientation distribution is expectedly isotropic. As the suspension is sheared at very low shear rates, to leading order, the vorticity component of the shear flow has no effect on the orientation distribution due to the isotropic distribution at equilibrium. The effect of the extensional component of the flow is to rotate the particle away from the compressional axis towards an alignment with the extensional axis. As a consequence, the probability near the compressional axis is reduced, while the probability near the extensional axis is enhanced¹⁴. The higher order approximations result from the vorticity as well as the extensional component of the flow¹⁴. In particular, the effect of the vorticity component of the flow is to rotate the distorted orientation distribution clockwise, such the probability maxima in the ODF shifts closer to the velocity axis, while the probability minima shifts closer to the gradient axis.

It is evident that the ODF $P(\varphi)$ in the present effort exhibits some trends similar to that in suspensions at infinite dilution. However, the mechanism of the distortion of the ODF

upon the onset of shear is very different in the two cases. First of all, we remind the reader that the effective single particle resistance tensor \mathbf{R}_0 of dicolloids in FLD is diagonal, which is qualitatively similar to the resistance tensor of an isolated sphere. Hence a single dicolloid by itself cannot exhibit a preferred alignment with any axis upon being subjected to shear. So, the distortion of the ODF in the present case clearly results from particle-particle interactions, which are expected to dominate anyway in concentrated suspensions. The precise mechanism of this distortion is easily understood with the help of a highly idealized example presented below.

Consider a single slender axisymmetric particle subjected to extensional flow, as shown in Fig. (12). This single particle by itself cannot rotate upon being subjected to extensional flow due to reasons discussed above. Now consider a second particle, which for simplicity is taken as a relatively small sphere in Fig. (12). The sphere, to first approximation, will move along the streamlines and consequently “collide” with the slender body causing it to rotate clockwise towards the extensional axis. It is easy to see that this will be case for most, if not all, starting positions of the second particle. Thus, in this idealized case, we see that the effect of particle collisions on the orientation dynamics of the slender body is much the same as that of slender body by itself in the extensional flow. By analogy of the orientation behavior at infinite dilution in Brenner¹⁴, we may expect an enhanced orientation probability along the extensional axis and a reduced orientation probability along the compressional axis at low shear rates in the present case as well. This is obviously the case here (see Fig. 11). Furthermore, at higher shear rates (Pe), the distorted ODF is expected to rotate clockwise so as to shift the probability maxima closer to the velocity axis and the probability minima closer to the gradient axis. This again is very similar to the observations in the present effort. However, there are some additional features in the ODF $P(\varphi)$ not resolved yet. At $Pe = 10$ in the higher volume fraction suspensions of both the homonuclear and the fused-dumbbell particles, the depth of the minima as well as the height of the maxima of $P(\varphi)$ decreases from the corresponding values at $Pe = 1$; see Figs. 11(b) and 11(e). It appears that this behavior results due to the formation of weak string like ordering around $Pe = 10$, particularly in suspensions of homonuclear particles. An obvious consequence of the presence of string like ordering will be to reduce the collision frequency between the particles, which, as discussed above, is a key driver of the distortion in the ODF. Yet another feature of the ODF $P(\varphi)$ in fused-dumbbell particle suspensions at high volume fractions and high shear rates is that it continues to display a decrease in the height of probability maxima and the depth of probability minima with increasing Pe (Fig. 11e). This cannot result from a string like ordering transition, as the microstructure is completely disordered in these suspensions at high shear rates (see Sec. 3.1). A likely origin of this behavior could be the hydrocluster mechanism proposed by Egres et al.¹⁶ – at high shear rates, large clusters of particles are typically formed, and these clusters of particles are expected to have a lower degree of anisotropy than the individual particles themselves. It is likely that the formation of more spherical clusters will result in a

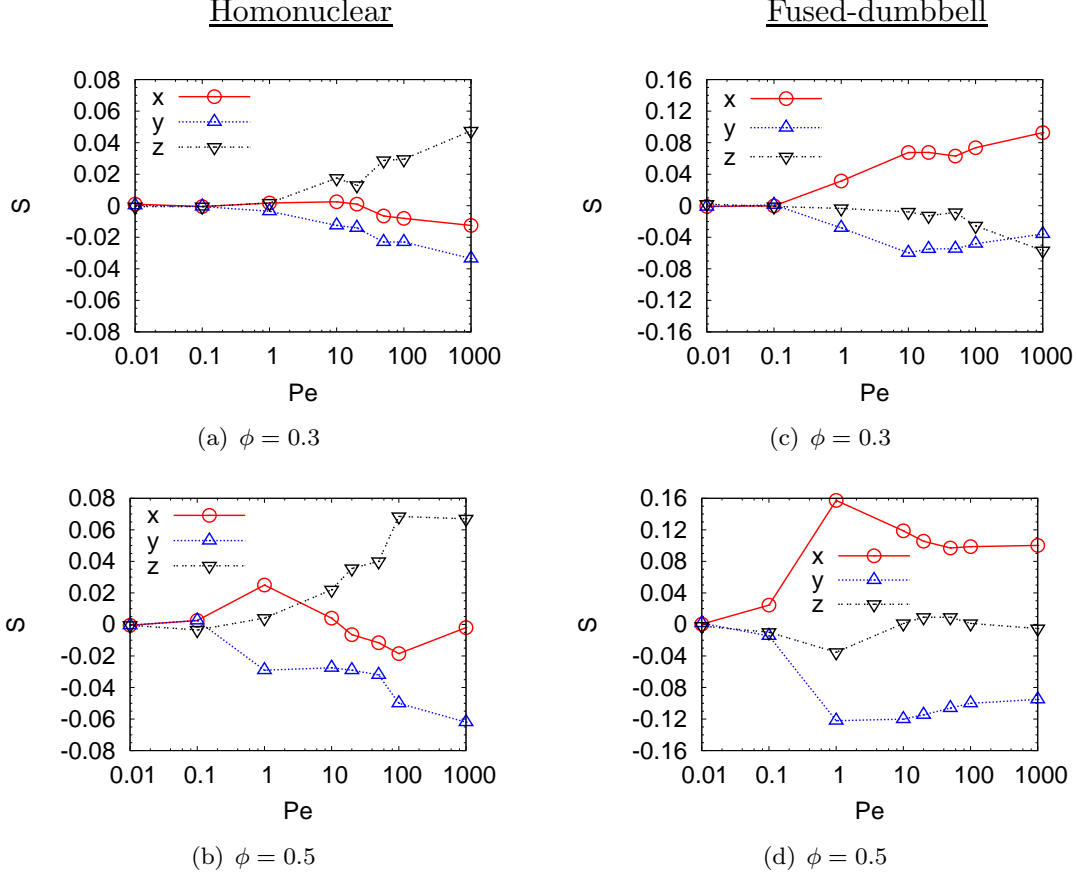


Figure 13: Orientation order parameters as a function of shear rate for (a) and (b) homonuclear particles and (c) and (d) fused-dumbbell particles at two different volume fractions ($\phi = 0.3$ and $\phi = 0.5$).

reduced distortion of the ODF. Lastly, we note that the trends in $\Delta\varphi_m$ follows directly from the corresponding trends in the ODF $P(\varphi)$, and hence will not be explicitly discussed here.

3.2.3 Orientation order parameters

We discussed above the orientation distribution functions $P(\theta)$ and $P(\varphi)$. These measures are particularly useful for gaining a mechanistic understanding of the orientation behavior. However, a more natural way of presenting the orientation results is to quantify the particle alignment with the three coordinate axes: velocity (x), gradient (y), and vorticity (z). With this goal, we present the results for the orientation order parameters S_{xx} , S_{yy} , and S_{zz} below.

Figures 13(a) and 13(b) respectively show the orientation order parameters in $\phi = 0.3$ and $\phi = 0.5$ suspensions of homonuclear particles as a function of Pe . In $\phi = 0.3$ suspensions, at $Pe = 0.01$, all three orientation order parameters are nearly zero, consistent with a random orientation at this low shear rate. With increasing shear rates, S_{zz} is found to increase, indicating an increased vorticity alignment with increasing shear rate as discussed in Sec.

3.2.1. In contrast, S_{xx} as well as S_{yy} decreases with increasing shear rate; the decrease in S_{xx} is smaller than the decrease in S_{yy} . The decrease in S_{xx} and S_{yy} primarily result due to the increase in S_{zz} , which leaves a smaller fraction to be distributed between S_{xx} and S_{yy} . The fact that S_{xx} decreases slower than S_{yy} is a direct consequence of the orientation distribution in the φ coordinate – with increasing shear rate, flow alignment is favored at the expense of gradient alignment as discussed in Sec. 3.2.2. At the higher volume fraction of $\phi = 0.5$, the trends in orientation order parameters are very similar to the trends observed in $\phi = 0.3$ suspension – the order parameter S_{zz} increases with shear rate, while S_{yy} decreases with shear rate. The only difference is that, at $\phi = 0.5$, S_{xx} does not decrease monotonically with increasing shear rate as is the case in the $\phi = 0.3$ suspension. As noted above, the instances in which S_{xx} increases with shear rate results due to the enhanced flow alignment of the particle in the velocity-gradient plane at the expense of the gradient alignment; see Sec. 3.2.2.

We next consider the orientation order parameters for fused-dumbbell particles in $\phi = 0.3$ and $\phi = 0.5$ suspensions, which are shown in Figs. 13(c) and 13(d), respectively. In the $\phi = 0.3$ suspension, the order parameter S_{zz} decreases with increasing shear rate, which is the direct consequence of increasing $\Delta\theta_m$ with increasing shear rate; see Sec. 3.2.1. The order parameter S_{xx} monotonically increases with increasing Pe . This results both due to the monotonically increasing $\Delta\theta_m$ with increasing Pe , implying an increasing velocity–gradient alignment with increasing Pe , as well as a (nearly) monotonically increasing $\Delta\varphi_m$ with increasing shear rate, indicating an increasing flow alignment in the velocity–gradient plane. The order parameter S_{yy} initially decreases with increasing shear rate, which primarily results due to the increase in S_{xx} . However, with further increase in shear rate, S_{yy} is found to increase, which can be attributed to the orientation drift away from the vorticity axis at higher shear rates, essentially leaving a greater fraction to be distributed in the flow and the gradient direction. At the higher volume fraction of $\phi = 0.5$, the order parameter S_{zz} , consistent with the trends in $\Delta\theta_m$, initially decreases with increasing shear rates, but is then found to increase for $Pe > 1$ and subsequently levels off at near zero values at very high shear rates. The order parameter S_{xx} shows a non-monotonic behavior with increasing shear rate: it initially increases with increasing shear rate reaching a maxima at $Pe = 1$; thereafter, it decreases with further increase in shear rate and eventually levels off at the highest shear rates considered here. In conjunction with the non-monotonic S_{xx} , the variation in the order parameter S_{yy} with increasing shear rate is also non-monotonic, though in the opposite direction: S_{yy} initially decreases with increasing shear rate, and thereafter it increases before it levels off at the high shear rate plateau. The non-monotonic variation in S_{xx} (or S_{yy}) with shear rate primarily results from the corresponding non-monotonic variation of $\Delta\varphi_m$ with shear rate. As discussed in Sec. (3.2.2), the non-monotonic variation in $\Delta\varphi_m$ perhaps results from two distinct mechanisms – first is the appearance of a weak string like ordering around $Pe = 10$, and second is the formation of hydroclusters¹⁶ at high shear rates. It is interesting to note that both of these mechanisms have the same apparent effect of causing a reduction in the flow alignment of the

particles.

4 Conclusions

In this study we investigated the orientation and microstructure in sheared Brownian suspensions of hard dicolloidal particles. Studies were conducted for a wide range of volume fractions ($0.3 \leq \phi \leq 0.5$) and shear rates ($0 \leq Pe \leq 1000$) in suspensions of homonuclear particles (aspect ratio 1.1) and fused-dumbbell particles (aspect ratio 1.5). The microstructure was found to lack a long range order at all volume fractions, though evidence of a weak string like ordering was apparent in suspensions of homonuclear particles at high volume fractions and at intermediate to high shear rates. The orientation distribution was found to be random at low shear rates. At the higher shear rates, homonuclear particles exhibited enhanced vorticity alignment at all volume fractions; fused-dumbbell particle suspensions, in contrast, exhibited reduced vorticity alignment at low volume fractions, and a negligible shift relative to the vorticity axis at higher volume fractions. The orientation distribution in the velocity–gradient plane indicated an increased flow alignment with increasing volume fractions for both particle shapes; flow alignment also increased with increasing shear rates at low volume fractions, but not necessarily at higher volume fractions. These observations on the orientation distribution were consistently resolved in the light of previous studies on Brownian and non-Brownian suspensions.

References

- [1] A. van Blaaderen. Colloids get complex. *Nature*, 439:545–546, 2006.
- [2] S. Yang, S. Kim, J. Lima, and G. Yi. Synthesis and assembly of structured colloidal particles. *Journal of Materials Chemistry*, 18:2177–2190, 2008.
- [3] S.C. Glotzer and M.J. Solomon. Anisotropy of building blocks and their assembly into complex structures. *Nature Materials*, 6:557–562, 2007.
- [4] S. Mitragotri and J. Lahann. Physical approaches to biomaterial design. *Nature Materials*, 8:15–23, 2008.
- [5] A. Kumar and M. D. Graham. Margination and segregation in confined flows of blood and other multicomponent suspensions. *Soft Matter*, 2012. doi: 10.1039/C2SM25943E.
- [6] P.M. Johnson, C.M. van Kats, and A. van Blaaderen. Synthesis of colloidal silica dumbbells. *Langmuir*, 21(24):11510–11517, 2005.
- [7] E.B. Mock, H. De Bruyn, B.S. Hawkett, R.G. Gilbert, and C.F. Zukoski. Synthesis of anisotropic nanoparticles by seeded emulsion polymerization. *Langmuir*, 22(9):4037–4043, 2006.

- [8] J.W. Kim, R.J. Larsen, and D.A. Weitz. Synthesis of nonspherical colloidal particles with anisotropic properties. *Journal of American Chemical Society*, 128(44):14374–14377, 2006.
- [9] A. Kumar and J. J. L. Higdon. Dynamics of the orientation behavior and its connection with rheology in sheared non-brownian suspensions of anisotropic dicolloidal particles. *Journal of Rheology*, 55:581–626, 2011.
- [10] G.B. Jeffery. The motion of ellipsoidal particles immersed in a viscous fluid. *Proceedings of the Royal Society of London. Series A*, 102(715):161–179, 1922.
- [11] F.P. Bretherton. The motion of rigid particles in a shear flow at low reynolds number. *Journal of Fluid Mechanics*, 14:284–304, 1962.
- [12] L. G. Leal and E. J. Hinch. The effect of weak brownian rotations on particles in shear flow. *Journal of Fluid Mechanics*, 46:685–703, 1971.
- [13] EJ Hinch and LG Leal. The effect of brownian motion on the rheological properties of a suspension of non-spherical particles. *Journal of Fluid Mechanics*, 52:683–712, 1972.
- [14] H. Brenner. Rheology of a dilute suspension of axisymmetric brownian particles. *International Journal of Multiphase Flow*, 1:195–341, 1974.
- [15] Q. Meng and J.J.L. Higdon. Large scale dynamic simulation of plate-like particle suspensions. part ii: Brownian simulation. *Journal of Rheology*, 52:37–65, 2008.
- [16] R.G. Egres, F. Nettesheim, and N.J. Wagner. Rheo-sans investigation of acicular-precipitated calcium carbonate colloidal suspensions through the shear thickening transition. *Journal of Rheology*, 50:685–709, 2006.
- [17] E. S. G. Shaqfeh and D. L. Koch. The effect of hydrodynamic interactions on the orientation of axisymmetric particles flowing through a fixed bed of spheres or fibers. *Physics of Fluids*, 31(4):728–743, 1988.
- [18] A. Sierou and J.F. Brady. Rheology and microstructure in concentrated noncolloidal suspensions. *Journal of Rheology*, 46:1031–1056, 2002.
- [19] L.G. Leal. The slow motion of slender rod-like particles in a second-order fluid. *Journal of Fluid Mechanics*, 69:305–337, 1975.
- [20] A. Kumar and J. J. L. Higdon. Origins of the anomalous stress behavior in charged colloidal suspensions under shear. *Physical Review E*, 82:051401, 2010.
- [21] A. Kumar. *Microscale dynamics in suspensions of non-spherical particles*. PhD thesis, University of Illinois at Urbana-Champaign, 2010.

- [22] A. Sierou and J.F. Brady. Accelerated stokesian dynamics simulations. *Journal of Fluid Mechanics*, 448:115–146, 2001.
- [23] A. Kumar and J. J. L. Higdon. Particle Mesh Ewald Stokesian dynamics simulations for suspensions of non-spherical particles. *Journal of Fluid Mechanics*, 675:297–335, 2011.
- [24] R.C. Ball and J.R. Melrose. A simulation technique for many spheres in quasi-static motion under frame-invariant pair drag and brownian forces. *Physica A*, 247:444–472, 1997.
- [25] A. J. Banchio and J. F. Brady. Accelerated stokesian dynamics: Brownian motion. *The Journal of chemical physics*, 118:10323, 2003.
- [26] P R Schunk, F. Pierce, J B Lechman, A M Grillet, H. Weiss, C. Stoltz, D R Heine, et al. Performance of mesoscale modeling methods for predicting rheological properties of charged polystyrene/water suspensions. *Journal of Rheology*, 56:353–384, 2012.
- [27] N. Kern and D. Frenkel. Fluid–fluid coexistence in colloidal systems with short-ranged strongly directional attraction. *The Journal of chemical physics*, 118:9882, 2003.
- [28] W.B. Russel, D.A.Saville, and W.R. Schowalter. *Colloidal Dispersions*. Cambridge University Press, 1989.
- [29] D.R. Foss and J.F. Brady. Structure, diffusion and rheology of brownian suspensions by stokesian dynamics simulation. *Journal of Fluid Mechanics*, 447:167–200, 2000.
- [30] Y. Saad. *Iterative Methods for Sparse Linear Systems*. Society for Industrial and Applied Mathematics, 2003.
- [31] C. Vega, E.P.A. Paras, and P. A. Monson. On the stability of the plastic crystal phase of hard dumbbell solids. *Journal of Chemical Physics*, 97(11):8543–8548, 1992.
- [32] R.J. Speedy. Pressure of the metastable hard-sphere fluid. *Journal of Physics Condensed Matter*, 9(41):8591–8599, 1997.
- [33] P. Bolhuis and D. Frenkel. Tracing the phase boundaries of hard spherocylinders. *Journal of Chemical Physics*, 106(2):666–687, 1997.
- [34] J.F. Brady and J.F. Morris. Microstructure of strongly sheared suspensions and its impact on rheology and diffusion. *Journal of Fluid Mechanics*, 348:103–139, 1997.
- [35] B. J. Ackerson. Shear induced order and shear processing of model hard sphere suspensions. *Journal of rheology*, 34:553, 1990.
- [36] L.B. Chen, M.K. Chow, B.J. Ackerson, and C.F. Zukoski. Rheological and microstructural transitions in colloidal crystals. *Langmuir*, 10:2817–2829, 1994.

- [37] M.K. Chow and C.F. Zukoski. Nonequilibrium behavior of dense suspensions of uniform particles: Volume fraction and size dependence of rheology and microstructure. *Journal of Rheology*, 39(1):33–59, 1995.
- [38] E.B. Mock and C.F. Zukoski. Investigating microstructure of concentrated suspensions of anisotropic particles under shear by small angle neutron scattering. *Journal of Rheology*, 51(3):541–559, 2007.